AIMS Mathematics, 11(4): 10159–10174.
DOI: 10.3934/math.2026419
Received: 10 December 2025
Revised: 28 March 2026
Accepted: 31 March 2026
Published: 14 April 2026

https://www.aimspress.com/journal/Math

Research article

Efficient multigrid method for dense regularization in fractional-order image deblurring

Shahbaz Ahmad[1], **Shahid Saleem**[2], **Abid Iqbal**[3] **and Saad Arif**[4,*]

[1] Abdus Salam School of Mathematical Sciences, Government College University, Lahore, 54600, Pakistan
[2] Department of Mathematics, The University of Chenab, Gujrat, 50700, Pakistan
[3] Department of Computer Engineering, College of Computer Sciences and Information Technology, King Faisal University, Al-Ahsa, 31982, Saudi Arabia
[4] Department of Mechanical Engineering, College of Engineering, King Faisal University, Al-Ahsa, 31982, Saudi Arabia

* **Correspondence:** Email: sarif@kfu.edu.sa.

Abstract: Fractional-order models have emerged as powerful tools in real-world image processing, offering enhanced edge preservation and improved reconstruction quality compared to traditional integer-order methods. The total fractional-order variation (TFOV) model is employed in this work to enhance the quality of deblurred images, as it is well known for its ability to preserve edges and mitigate the staircase effect. However, the dense regularization matrix associated with the TFOV model poses challenges in the design of efficient numerical algorithms. To overcome this issue, a robust and efficient multigrid method specifically designed to address matrix density is proposed. This approach develops multigrid solvers tailored for image deblurring problems governed by TFOV regularization under Dirichlet boundary conditions. Using a Lagrange multiplier framework, the optimality system for the image deblurring problem is derived, linking the state, adjoint, and intensity variables. Multigrid techniques on staggered grids are explored, employing a coarsening factor of three to generate a nested hierarchy that facilitates simplified intergrid transfer operations. Within this framework, a preconditioned conjugate gradient method is used as a smoother. Numerical experiments confirm the accuracy and efficiency of the proposed multigrid approach. These results highlight the practical viability of multigrid solvers for dense fractional regularization and reinforce their usefulness in large-scale image restoration tasks.

Keywords: image deblurring; fractional-order variation; multigrid methods; inverse problems; image restoration; preconditioned conjugate gradient; staggered grids; edge preservation
Mathematics Subject Classification: 94A08, 65N55, 68U10, 65N12

1. Introduction

Image deblurring (ID) has attracted significant interest in various fields such as remote sensing [1], robot vision [2], medical image processing [3], astronomical imaging, virtual reality, and numerous other domains within image processing. The fundamental mathematical relationship between the original image, denoted as u, and its blurred counterpart, represented as z, can be expressed as follows:

$$z = \mathbf{K}u + \epsilon, \tag{1.1}$$

where $\mathbf{K}$ is an operator that causes the blur, and ϵ represents a noise function. The action of $\mathbf{K}$ on u is defined as

$$(\mathbf{K}u)(x) = \int_{\mathcal{D}} k(x, y)u(y)\, dy, \quad \mathbf{x} \in \mathcal{D}, \tag{1.2}$$

where $k(x, y) = \phi(x-y)$ is known as a point spread function (PSF) or a blurring kernel with a translation-invariant property [4]. The deconvolution problem involves recovering $\mathbf{K}$ and u from z [5]. When the operator $\mathbf{K}$ is known, the process is termed non-blind deconvolution [6]. If the blurring operator $\mathbf{K}$ is unknown, the process is termed blind deconvolution [7]. This paper primarily focuses on non-blind deconvolution. The operator $\mathbf{K}$ is compact, therefore, retrieving u from z presents challenges, rendering problem (1.1) an unstable inverse problem [8]. To address this issue, extensive research has been devoted to energy minimization models, which have garnered considerable attention for solving ID problems in recent decades [9].

$$\min_{u\in\mathcal{D}} \int_{\mathcal{D}} (k * u - z)^2 d\mathcal{D} + \mu R(u). \tag{1.3}$$

Here, $\mathcal{D}$ denotes a constrained set, $R(u)$ represents a regularization functional, and $\mu > 0$ serves as a smoothing parameter that controls the trade-off between data fidelity and regularization terms [10]. Additionally, $*$ represents a two-dimensional convolution operator. Restoring blurred images using non-blind deconvolution is a challenging task. To address this, various deconvolution methods incorporate image priors to stabilize the solution. One widely used approach is the Tikhonov regularization model [11]:

$$\min_{u\in\mathcal{D}} \int_{\mathcal{D}} (k * u - z)^2 d\mathcal{D} + \mu \int_{\mathcal{D}} |u| d\mathcal{D}. \tag{1.4}$$

The Tikhonov model [12] tends to overly smooth image results due to its least-squares formulation. To better preserve edges, the total variation (TV) model has gained popularity. It is known for its edge-preserving properties and is widely used in nonlinear energy minimization for ID [13]:

$$\min_{u\in\mathcal{D}} \int_{\mathcal{D}} (k * u - z)^2 d\mathcal{D} + \mu \int_{\mathcal{D}} |\bigtriangledown u|_\eta d\mathcal{D}, \tag{1.5}$$

where $|\bigtriangledown u|_\eta = \sqrt{u_x^2 + u_y^2 + \eta}$. The parameter $\eta > 0$ is introduced to ensure that the functional remains differentiable at zero. The TV model [14] offers several advantages but suffers from a notable drawback. It tends to transform smooth regions into blocky structures, producing a staircase effect. To address this limitation, total fractional-order variation (TFOV)-based models have been proposed.

These models, as explored in [15], provide an alternative approach to reduce staircase artifacts in reconstructed images:

$$\min_{u\in\mathcal{D}} \int_{\mathcal{D}} (k * u - z)^2 d\mathcal{D} + c \int_{\mathcal{D}} \sqrt{|\nabla^{\alpha} u|^2 + \eta^2} d\mathcal{D}, \tag{1.6}$$

where α denotes the order of the unified fractional derivative [16]:

$$D_{\theta}^{\alpha} g(t) = \lim_{h\to 0^+} h^{-\alpha} \sum_{n=-\infty}^{\infty} (-1)^n \frac{\Gamma(\alpha+1)}{\Gamma\left(\frac{\alpha+\theta}{2} - n + 1\right)\Gamma\left(\frac{\alpha-\theta}{2} + n + 1\right)} g(t - nh). \tag{1.7}$$

Here, θ is a parameter often referred to as the skewness (or asymmetry) parameter, as it determines the symmetry of the derivative (as observed in the frequency response), and h is a positive real number. TFOV-based regularization models are recognized for their remarkable efficiency. These models preserve edge sharpness in reconstructed images while mitigating unwanted staircase artifacts.

Recently, TFOV-based image processing models have gained significant attention. Studies in areas such as image edge detection [17], denoising [18], and reconstruction [19] provide key insights. For instance, Tian et al. [20] introduced a fractional-order adaptive technique for image denoising, while Zhang et al. [21] demonstrated the ability of the TFOV model to reduce the staircase effect in image restoration. Mathieu et al. [22] proposed an edge detection technique based on fractional differentials, enhancing texture and edge details.

These studies indicate that, compared to first- and second-order total variation methods, TFOV more effectively represents image textures. Recently, Guo et al. [23] and Fairag et al. [24] incorporated TFOV models into ID, demonstrating their potential. However, applying these methods to blurred and noisy images presents two significant challenges: handling nonlinearity and solving large-scale matrix systems.

1.1. Related work

Considerable effort has recently been devoted to the development of multigrid methods for optimal control problems. Borzi and Schulz provide a comprehensive review in [25], along with additional references. In [26], C. Schauf et al. discussed techniques based on nonlinear multigrid methods specifically applied to total variation image denoising. Preconditioners based on multigrid techniques were developed for a linear-quadratic optimal control problem constrained by the Stokes system to accelerate the solution process, as described in [27]. The work in [28] introduced a robust multigrid method tailored for the Stokes control problem, demonstrating strong convergence with respect to both the regularization parameter and grid size.

1.2. Scope of the proposed work

Over the past two decades, nonlinear variational methods have attracted significant interest in the field of ID. Image reconstruction problems often involve complex regularization approaches such as TFOV. However, applying these techniques to large-scale noisy and blurred images presents two major challenges, despite their effectiveness in preserving edges and reducing blocky artifacts. The first challenge arises from the inherent nonlinearity of the models, stemming from the construction of the associated Euler–Lagrange equations. The second challenge is related to solving the large-scale

systems generated by their discretization, which involve dense matrices. This paper primarily aims to address these two computational challenges.

To address these challenges, the approach presented in [29] is extended for ID with TFOV-based constraints. Multigrid solvers are developed that employ a coarsening strategy with a factor of three on staggered grids. This strategy simplifies intergrid transfer operators, accelerates coarsening, and reduces the number of required levels. The focus is placed on developing tailored multigrid solvers for ID problems governed by TFOV under Dirichlet boundary conditions. An optimality system is established using a Lagrange multiplier framework, linking the state, adjoint, and intensity variables. By implementing a coarsening with a factor of three on staggered grids, a preconditioned conjugate gradient (PCG) method is employed as a smoothing scheme within this framework. The numerical investigations demonstrate that the proposed multigrid scheme provides improved reconstruction of blurred images when μ is not close to 0, compared to recent work [30].

The organization of the paper is as follows: The next section presents the minimization problem and characterizes its solution through the optimality system in a 2D computational domain. Section 3 describes the discretization of the optimality system, followed by Section 4, which details the proposed multigrid scheme. Section 5 presents the results of numerical experiments on the ID problem. Finally, the last section provides the conclusions.

2. Minimization problem for image deblurring

In this study, the ID problem is considered in a $2D$ bounded domain $\mathcal{D} \subset R^2$ with a Lipschitz boundary $\Gamma = \partial\mathcal{D}$. The functional for the ID problem, subject to TFOV-based constraints, is given by

$$J(u) = \frac{1}{2}\|ku - z\|^2 + \frac{\mu}{2}\|f\|^2. \tag{2.1}$$

This functional is minimized subject to the following conditions:

$$\nabla^\alpha u - f = 0, \tag{2.2}$$

$$u = 0 \ \text{ on } \quad \Gamma. \tag{2.3}$$

Here, $u \in H_0^1$ represents the intensity function, and μ denotes the regularization parameter.
The Lagrange framework [31] is adopted to describe the solution of problem (2.1)–(2.3). The associated Lagrangian functional to this optimization problem is expressed as

$$L(u, f, \lambda) = \frac{1}{2}\|ku - z\|^2 + \frac{\mu}{2}\|f\|^2 + \langle \nabla^\alpha u - f, \lambda\rangle$$

$$= \frac{1}{2}\|ku - z\|^2 + \frac{\mu}{2}\|f\|^2 - \langle \nabla^\alpha u, \lambda\rangle + \langle f, \lambda\rangle,$$

where $\lambda \in H_0^1(\mathcal{D})$ is the Lagrange multiplier, resulting in the following optimality system [24].
The state system is given by

$$\begin{cases} \nabla^\alpha u - f = 0, \\ u = 0 \quad \text{on} \quad \Gamma. \end{cases} \tag{2.4}$$

The adjoint system is given by

$$\begin{cases} k^*(ku - z) + \nabla^\alpha \lambda = 0, \\ \lambda = 0. \end{cases} \tag{2.5}$$

The optimality condition is

$$\mu f - \lambda = 0.$$

Here, $\lambda = \lambda(x, y)$, $f = f(x, y)$, and $u = u(x, y)$. This system defines the solution $(u, f) \in H_0^1(\mathcal{D}) \times L^2(\mathcal{D})$ of the ID problem with the Lagrange multiplier $\lambda \in H_0^1(\mathcal{D})$. The spaces $H^1(\mathcal{D})$ and $L^2(\mathcal{D})$ denote the Sobolev and standard Lebesgue spaces, respectively, with $|\cdot|H^1(\mathcal{D})$ and $|\cdot|L^2(\mathcal{D})$ as their corresponding norms. The usual inner product for $L^2(\mathcal{D})$ is denoted by $(\cdot, \cdot)$. It is assumed that $\mathcal{D}$ is convex. Additionally, $L_0^2(\mathcal{D})$ denotes the space of functions in $L^2(\mathcal{D})$ with zero mean:

$$L_0^2(\mathcal{D}) = \{\phi \in L^2(\mathcal{D}) : \int_{\mathcal{D}} \phi dx = 0\}. \tag{2.6}$$

The space $H_0^1(\mathcal{D})$ is defined as the subspace of $H^1(\mathcal{D})$ whose elements vanish on the boundary: $H_0^1(\mathcal{D}) = \{\psi \in H^1(\mathcal{D}) : \psi = 0 \text{ on } \partial\mathcal{D}\}$.

3. Discrete formulation of optimal system

This section describes the discretization of the optimality system using the unified fractional derivative [16] on staggered grids. Implementation details are presented, emphasizing the advantageous arrangement of optimization variables. A sequence of grids $\{\mathcal{D}_h\}_{h>0}$ is considered, defined as

$$\mathcal{D}_h = \{x \in \mathbf{R^2} : \mathbf{x_k} = \mathbf{kh_x}, \mathbf{y_l} = \mathbf{lh_y}, \mathbf{k}, \mathbf{l} \in \mathbf{Z}\} \cap \mathcal{D}.$$

The domain $\mathcal{D}$ is assumed to be rectangular, and the mesh step sizes h_x and h_y are selected such that the boundaries of $\mathcal{D}$ coincide with the grid lines. Staggered grids accommodate variables positioned on cell edges (horizontal or vertical) and at cell centers. These grid points are denoted by $\mathcal{D}_h^s$, where $s \in \{ev, eh, c\}$. For example, $\mathcal{D}_h^{ev}$ denotes grid points located at the centers of vertical cell edges. In this arrangement, grid points are separated by distances of h_x and h_y in the horizontal and vertical directions, respectively. The unified fractional derivative in discrete form [32] is used:

$$D_{x,\theta}^\alpha g(x_k, y_l) = \frac{1}{h^\alpha} \sum_{i=-M}^{M} \varphi_i^{(\alpha,\theta)} g(x_k - ih, y_l), \tag{3.1}$$

where

$$\varphi_i^{(\alpha,\theta)} = (-1)^i \frac{\Gamma(\alpha + 1)}{\Gamma\left(\frac{\alpha+\theta}{2} - i + 1\right)\Gamma\left(\frac{\alpha-\theta}{2} + i + 1\right)}. \tag{3.2}$$

From Eq (3.1), it can be observed that, along the x-direction, the first-order approximation of $D_{x,\theta}^\alpha g(x_k, y_l)$ at point (x_k, y_l) can be expressed as a linear combination of $N + 2$ values $({g^l}_0, {g^l}_1, ..., {g^l}_N, {g^l}_{N+1})$ with fixed y_l. After applying homogeneous boundary conditions to all N equations, the fractional derivatives in the x-direction in Eq (3.1) can be represented as follows:

$$\begin{bmatrix} D^\alpha g(x_1, y_l) \\ D^\alpha g(x_2, y_l) \\ \vdots \\ \vdots \\ D^\alpha g(x_N, y_l) \end{bmatrix} = \underbrace{\frac{1}{h^\alpha} \begin{bmatrix} {\varphi_0}^\alpha & {\varphi_1}^\alpha & {\varphi_2}^\alpha & \cdots & \varphi_{N-1}^\alpha \\ {\varphi_1}^\alpha & {\varphi_0}^\alpha & \ddots & \ddots & \varphi_{N-2}^\alpha \\ {\varphi_2}^\alpha & \ddots & \ddots & \ddots & \vdots \\ \vdots & \ddots & \ddots & {\varphi_1}^\alpha & \vdots \\ {\varphi_{N-1}}^\alpha & \cdots & {\varphi_{N-2}}^\alpha & \ddots & {\varphi_0}^\alpha \end{bmatrix}}_{M_N^\alpha} \begin{bmatrix} g_1^i \\ g_2^i \\ \vdots \\ \vdots \\ g_N^i \end{bmatrix}.$$

By applying the Gershgorin circle theorem, the matrix M_N^α is identified as symmetric and negative definite, forming a Toeplitz matrix [30]. Consequently, $-M_N^\alpha$ is positive definite. Let $U \in \mathbb{R}^{N\times N}$ represent the solution matrix at nodes $(kh_x; lh_y)$, where $k, l = 1, \ldots, N$ correspond to the spatial discretization nodes in the x and y directions. The solution vector U is represented by $\vec{u} \in \mathbb{R}^{N^2\times 1}$ in the ordered form. By a discrete and direct analogy to differentiation, u_x^α (α order derivative in x-direction) is given by

$$u_x^\alpha = (I_N \otimes C_N^\alpha)\vec{u} = C_x^\alpha \vec{u}. \tag{3.3}$$

Similarly, the fractional derivative ${u_y}^\alpha$ (α order derivative in y-direction) is given by

$$u_y^\alpha = (C_N^\alpha \otimes I_N)\vec{u} = C_y^\alpha \vec{u}, \tag{3.4}$$

where

$$u_x^\alpha = (u_{11}^\alpha, ..., u_{N1}^\alpha, u_{12}^\alpha, ..., u_{NN}^\alpha)^T, \quad u_y^\alpha = (u_{11}^\alpha, ..., u_{1N}^\alpha, u_{21}^\alpha, ..., u_{NN}^\alpha)^T. \tag{3.5}$$

Here, $\otimes$ denotes the Kronecker product, and $\vec{u} = u_{11}, u_{12}, ..., u_{NN}$. The α-order derivative ${u_x}^\alpha$ of $u(x, y)$ along all x-direction nodes in $\mathcal{D}$ can be represented by the matrix $C_N^\alpha \mathcal{U}$.

A grid index set (k, l) is considered, where $k = 1, \ldots, N_x + 1$ and $l = 1, \ldots, N_y$, covering all grid points including boundaries, arranged in lexicographic order starting from $(1, 1)$ (the bottom-left corner). The solution matrix $U \in \mathbb{R}^{N\times N}$ is defined at cell centers $(k+\frac{1}{2}, l+\frac{1}{2})$, f^x, while f^x and f^y denote the solutions at vertical and horizontal edges, respectively. The discretized state system is given by

$$f^x = (I_N \otimes C_N^\alpha) \text{ on } \mathcal{D}_h^{ev}, \tag{3.6}$$

$$f^y = (C_N^\alpha \otimes I_N) \text{ on } \mathcal{D}_h^{eh}. \tag{3.7}$$

The grid vertices are defined as $y_l = (l-1)h_y$ and $x_k = (k-1)h_x$. The value of the function u at cell centers is denoted by $u_{k+\frac{1}{2},l+\frac{1}{2}}$. The optimality conditions $\alpha f^x - \lambda^x = 0$ and $\alpha f^y - \lambda^y = 0$ determine the placement of variables on the grid. Specifically, u, λ^x, and f^x are defined on $\mathcal{D}_h^{ev}$, while f^y and λ^y are defined on $\mathcal{D}_h^{eh}$. Consequently, the discretized adjoint system is expressed as

$$(Ku - z)_{k+1/2,l+1/2} = \lambda^x \text{ on } \mathcal{D}_h^{ev}, \tag{3.8}$$

$$(Ku - z)_{k+1/2,l+1/2} = \lambda^y \text{ on } \mathcal{D}_h^{eh}. \tag{3.9}$$

The proposed approach, based on optimality conditions, establishes a direct relationship between state, adjoint, and intensity variables, eliminating the need for interpolation. Consequently, Eqs (3.10) and (3.11) define the discrete optimality system

$$\begin{cases} \alpha f_{k,l+\frac{1}{2}}^x - \lambda_{k,l+\frac{1}{2}}^x = 0, & \text{on } \mathcal{D}_h^{ev}, \\ \alpha f_{k+\frac{1}{2},l}^y - \lambda_{k+\frac{1}{2},l}^y = 0, & \text{on } \mathcal{D}_h^{eh}, \end{cases} \tag{3.10}$$

with boundary conditions

$$\begin{aligned} f^x_{k,l+\frac{1}{2}} &= 0 \quad \text{for } k = 1, N_x + 1, l = 1, ...N_y, \\ f^y_{k+\frac{1}{2},l} &= 0 \quad \text{for } l = 1, N_y + 1, k = 1, ...N_x, \\ \lambda^x_{k,l+\frac{1}{2}} &= 0 \quad \text{for } k = 1, N_x + 1, l = 1, ...N_y, \\ \lambda^y_{k+\frac{1}{2},l} &= 0 \quad \text{for } l = 1, N_y + 1, k = 1, ...N_x. \end{aligned} \tag{3.11}$$

4. Comprehensive multigrid methodology

A complete multigrid algorithm was developed to solve the discrete optimal system (3.6)–(3.11). During the development process, challenges were encountered due to the structure of staggered grids and the coupling between adjoint and state systems. It is well known that, in multigrid techniques, multiple discretization grids are utilized. Typically, these grids are generated by refining an initial coarse grid (as given in Figure 1), for example, by halving the mesh size, thereby creating an independent grid hierarchy. This configuration places the same types of variables at different spatial locations across hierarchy levels, which requires additional effort in constructing grid interpolation operators [33].

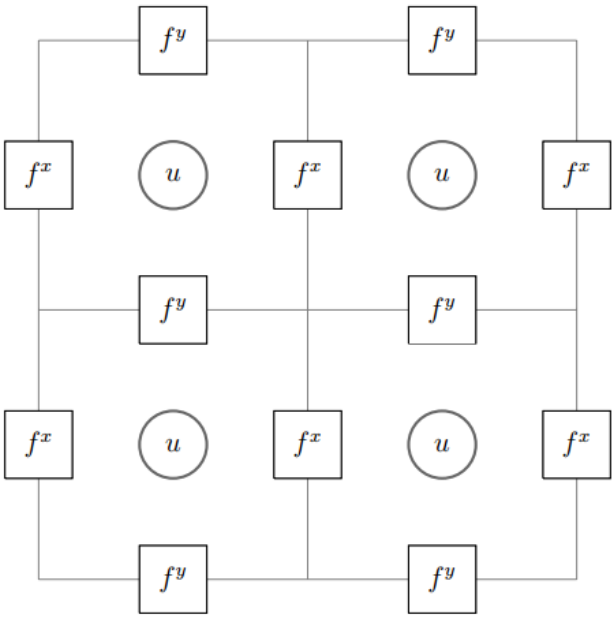

Figure 1. Coarsest staggered grid.

To overcome these challenges and restore the benefits of a nested grid sequence, a novel approach is proposed. Instead of the conventional refinement process, a nested sequence of grids is generated by tripling the mesh size from a given coarse grid, as illustrated in Figure 2. This observation is particularly significant in staggered-grid settings for the development of multigrid schemes in optimal control problems.

A hierarchy of nested grids, denoted by $\mathcal{D}_m$, is defined, where the mesh sizes are given by $h_{x_m} = \frac{h_{x_1}}{3^{m-1}}$

and $h_{y_m} = \frac{h_{y_1}}{3^{m-1}}$, for $m = 1, 2, \ldots, \bar{N}$. The coarsest grid corresponds to $m = 1$, while the finest grid is associated with level $m = \bar{N}$. The index m is used to denote all functions and operators defined on $\mathcal{D}_m$. In this framework, the spatial location of a variable X_{KL}^{m-1} on the coarser grid $\mathcal{D}_{m-1}$ corresponds exactly to the location of a variable X_{kl}^{m} on the finer grid $\mathcal{D}_m$, as shown in Figure 2.

- $u_{K+1/2,L+1/2}^{m-1}$ corresponds to u_{kl}^{m} for $k = 3K - 1, l = 3J - 1$;
- $(f^x)_{I+1/2,J}^{m-1}$ corresponds to $(f^x)_{kl}^{k}$ for $k = 3K - 1, l = 3L - 2$;
- $(f^y)_{K,L+1/2}^{m-1}$ corresponds to $(f^y)_{kl}^{m}$ for $k = 3K - 2, l = 3L - 1$;
- $\lambda_{K,L+1/2}^{m-1}$ corresponds to λ_{kl}^{m} for $k = 3K - 2, l = 3L - 1$.

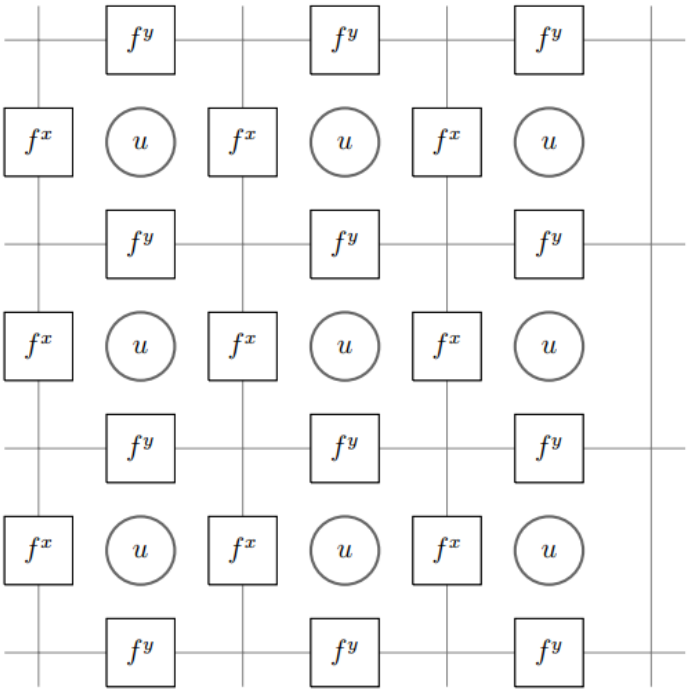

Figure 2. Coarse and fine grids.

Coarsening by a factor of three produces a nested sequence of staggered grids and simplifies the implementation of bilinear interpolation. Accordingly, bilinear interpolation is applied in the space $\mathcal{U}_m$, where $u^m : \mathcal{D}_m^{\text{ev}} \to R$ for $m = 1$ to $\bar{N}$. The transition between two grids, $\mathcal{D}_m$ and $\mathcal{D}_{m-1}$, is performed using a consistent prolongation operator $P_{m-1}^{m} : \mathcal{U}_{m-1} \to \mathcal{U}_m$, constructed under the assumption of bilinear finite elements over each rectangular cell.

In the context of a threefold coarsening (Figure 2), coarse-grid points coincide with fine-grid points. Therefore, a direct injection operator, denoted as $P_{m}^{m-1} : \mathcal{U}_m \to \mathcal{U}_{m-1}$, is employed to transfer residuals and solution variables from finer to coarser grids. However, the use of a straightforward injection

operator as a restriction operator is not needed. This choice is consistent with the factor-of-three coarsening strategy.

4.1. Multigrid algorithms

The proposed approach is introduced through two methods: the full multigrid (FMG) method and the full approximation scheme (FAS). The FAS method is particularly effective for solving optimization problems, as it utilizes state, adjoint, and intensity variables that are available at all grid levels. This feature is essential for addressing nonlinear and constrained control problems. Furthermore, computational efficiency is enhanced by integrating the FMG scheme, which combines the FAS scheme with a nested iteration strategy. The optimality system (2.1)–(2.5) for the unknown variables $X_m = (u_m, \lambda_m, f_m)$ is considered at the discrete level and can be expressed compactly as $A_m(X_m) = F_m$.

The correction e_m to an approximate solution $\tilde{X}_m$ is defined as the solution of

$$A_m\left(\tilde{X}_m + e_m\right) - A_m\left(\tilde{X}_m\right) = r_m, \tag{4.1}$$

where associated residual is $r_m = F_m - A_m\left(\tilde{X}_m\right)$. Moving to the coarser grid $\mathcal{D}_{m-1}$ and representing $\tilde{X}_m + e_m$ on it, $X_{m-1} := P_m^{m-1}\tilde{X}_m + e_{m-1}$ is used. Here, e_m is represented by a coarse function e_{m-1} due to its smoothness from S_m. The corresponding FAS equation is derived as

$$A_{m-1}(X_{m-1}) = P_m^{m-1}\left(F_m - A_m\left(\tilde{X}_m\right)\right) + A_{m-1}\left(P_m^{m-1}\tilde{X}_m\right). \tag{4.2}$$

This can also be written as $A_{m-1}(X_{m-1}) = P_m^{m-1}F_m + \tau_m^{m-1}$, where $\tau_m^{m-1} = A_{m-1}\left(P_m^{m-1}\tilde{X}_m\right) - P_m^{m-1}A_m\left(\tilde{X}_m\right)$ denotes the fine-to-coarse defect.

Convergence implies $X_{m-1} = P_m^{m-1}X_m$. Solving the coarse grid Eq (4.2) yields X_{m-1}, and its combination with Eq (4.1) provides $e_{m-1} = X_{m-1} - P_m^{m-1}\tilde{X}_m$. The corrected fine-grid approximation is then given by

$$X_m = \tilde{X}_m + P_{m-1}^m\left(X_{m-1} - P_m^{m-1}\tilde{X}_m\right). \tag{4.3}$$

Here, P_{m-1}^m denotes the coarse-to-fine transfer operator. To reduce the error after coarse-grid correction, i_2 post-smoothing iterations are performed.

The FAS algorithm is summarized below.

Algorithm 3.1 *FAS* (i_1, i_2) for solving $A_m(X_m) = F_m$.

1. If $m = 1$, compute the exact solution of $A_m(X_m) = F_m$;
2. perform the pre-smoothing steps on the fine grid: $X_m^{(n)} = S_m\left(X_m^{(n-1)}, F_m\right), n = 1, \ldots, i_1$;
3. compute the residual: $r_m = F_m - A_m\left(X_m^{(i_1)}\right)$;
4. refine the residual: $r_{m-1} = P_m^{m-1}r_m$;
5. Set $X_{m-1} = P_m^{m-1}X_m^{(i_1)}$;
6. set $F_{m-1} = r_{m-1} + A_{m-1}(X_{m-1})$
7. call i times $MG(i_1, i_2)$ to solve $A_{m-1}(X_{m-1}) = F_{m-1}$;
8. coarse-grid correction: $X_m^{(i_1+1)} = X_m^{(i_1)} + P_{m-1}^m\left(X_{m-1} - P_m^{m-1}X_m^{(i_1)}\right)$;
9. post-smoothing steps on the fine grid: $X_m^{(n)} = S_m\left(X_m^{(n-1)}, F_m\right), n = i_1 + 2, \ldots, i_1 + i_2 + 1$.

When solving nonlinear problems, initiating the iterative process with a strong initial estimate is essential. Within the multigrid framework, this can be achieved naturally using a nested iteration strategy. The solution process begins on a coarse grid level $n = K < M$, where the problem $A_n(X_n) = F_n$ with $n = K$ is relatively easy to solve. The obtained solution is then interpolated to the next finer level as an initial approximation to solve $A_{n+1}(X_{n+1}) = F_{n+1}$, and is denoted by $X_{n+1} = I_n^{n+1} X_n$.

Subsequently, the FAS procedure is applied at level $n+1$. This approach, known as nested iteration, improves convergence by providing high-quality initial guesses. By combining multigrid cycles with nested iteration, the full FMG method is obtained. The FMG method is more efficient than standard multigrid cycles, as it enhances the initial approximation at each level. The FMG algorithm is summarized below.

Algorithm 3.2 FMG to solve $A_N(X_N) = F_N$.

1. For $n = M < N$ choose an initial estimate u_n;
2. if $n < N$ then interpolate to the next finer working level $\tilde{X}_{n+1} = n_n^{n+1} X_n$;
3. utilize FAS for solving $A_{N+1}(X_{N+1}) = F_{N+1}$, beginning with $\tilde{X}_{n+1}$;
4. set $n = n + 1$; if $n < N$ proceed to step 2; else stop.

5. Numerical experiments

This section presents numerical experiments demonstrating the effectiveness of the proposed algorithm for ID. For all numerical computations, MATLAB software was utilized on a system equipped with an AMD A12-9720P RADEON R7 processor (12 compute cores, 4C+8G, 2.70 GHz). Based on the results reported in [24], the parameters $\mu = 1 \times 10^{-8}$, $\alpha = 1.8$, and $\lambda = 0.1$ were selected, as they yield superior performance. For all examples, the stopping criterion for the numerical method was defined using a tolerance of $tol = 1 \times 10^{-7}$. The kernel $ke\text{-}gen(n_x, r, \sigma)$ [34] was employed for numerical calculations. This kernel represents a circular Gaussian filter of size $n_x \times n_y$ with standard deviation σ and radius r. Figure 3 illustrates the kernel $ke\text{-}gen(120, 40, 4)$.

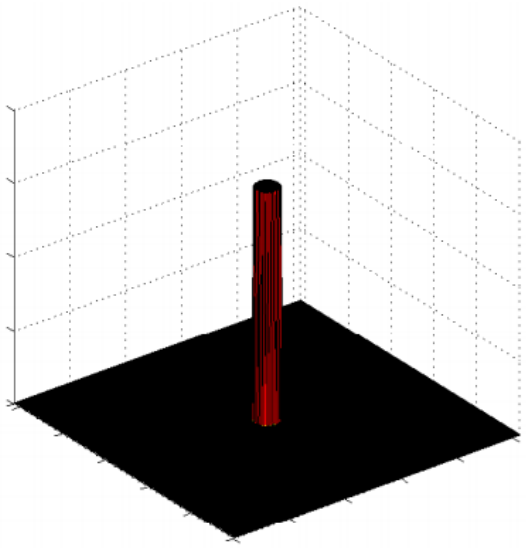

Figure 3. The blurring kernel $ke\text{-}gen(120, 40, 4)$.

The quality of image reconstruction was evaluated using the peak signal-to-noise ratio (PSNR) [35], where higher PSNR values indicate better restoration quality. The efficiency of the algorithm was assessed based on the iteration count. In Examples 1–3, the proposed method was applied to image deblurring problems using benchmark images, including Cameraman, Goldhill, and Moon. Computations were performed on grid sizes of 64, 128, 256, and 512. The results were compared with the conjugate gradient method (CGM) and the two-level method (TLM) [24].

Example 1. In this example, the Goldhill image was used. This image exhibits significant texture characteristics. The blurring process was performed using the *ke-gen*$(N, 100, 5)$ kernel. A comparison of the proposed method with CGM and TLM is presented. The restored images are shown in Figure 4, while Table 1 provides details of the experiment. Figure 4 presents a comprehensive representation of the Goldhill image, including five components corresponding to different processing stages. Each subfigure has a resolution of 512×512 pixels. The numerical experiments indicate that the proposed method achieves superior reconstruction quality compared to CGM and TLM. Table 1 summarizes the experimental results.

Example 2. In this example, the Cameraman image was used, and the blurring process was applied using the *ke-gen*$(N, 100, 5)$ kernel. The Cameraman image contains complex structures with intricate texture details. Figure 5 presents a comprehensive representation of the Cameraman image, including five components corresponding to different processing stages. Each subfigure has a resolution of 512×512 pixels. The numerical experiments indicate that the proposed method achieves superior reconstruction quality compared to CGM and TLM. Table 2 summarizes the experimental results.

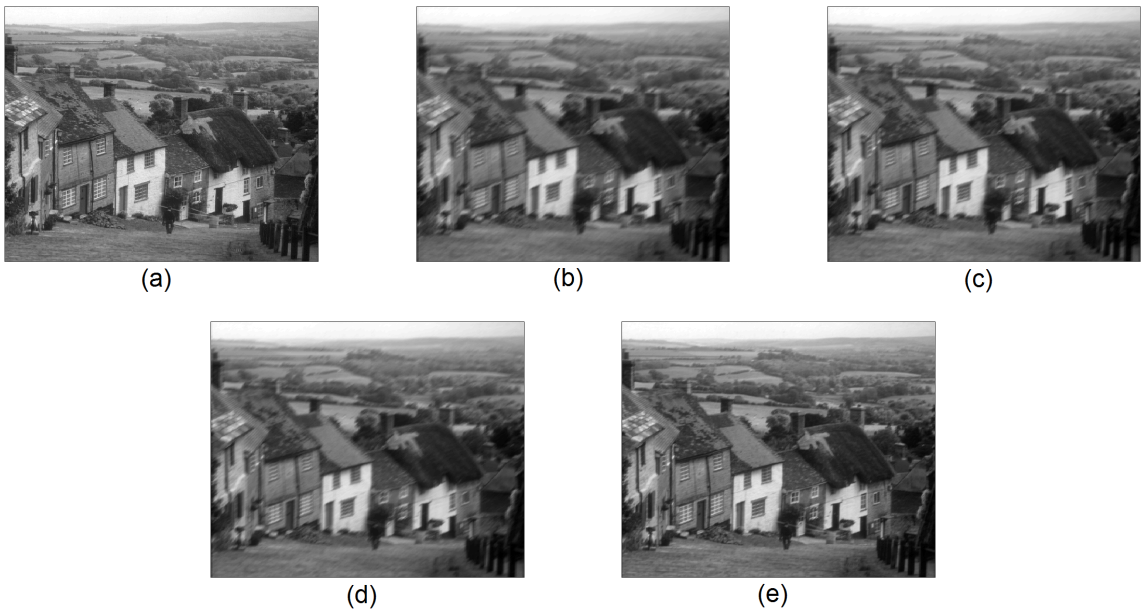

Figure 4. Goldhill image: (a) The original image, (b) the blurred image, (c) the image recovered using CGM, (d) the image recovered using TLM method, and (e) the image recovered using the multigrid method.

Table 1. PSNR, iteration count, and CPU time comparison for the Goldhill image.

Goldhill		CGM		Residue		TLM		Residue		Multigrid		Residue
Size	PSNR	Iter.	CPU (s)		PSNR	Iter.	CPU (s)		PSNR	Iter.	CPU (s)	
64×64	59.3465	10	29.5341	1.1655×10^{-8}	27.3423	10	8.3793	7.6757×10^{-8}	61.0319	6	8.3793	9.7252×10^{-9}
128×128	56.3652	15	40.5428	1.1983×10^{-8}	28.2120	17	15.3573	7.5644×10^{-8}	58.2197	8	15.3573	9.7927×10^{-9}
256×256	51.8512	97	195.2980	1.2543×10^{-8}	29.8744	104	72.5472	7.7644×10^{-8}	53.3145	82	72.5472	9.6872×10^{-9}
512×512	45.7623	182	464.1948	1.2987×10^{-8}	31.2723	184	202.1632	7.5636×10^{-8}	47.1376	143	202.1632	9.6823×10^{-9}

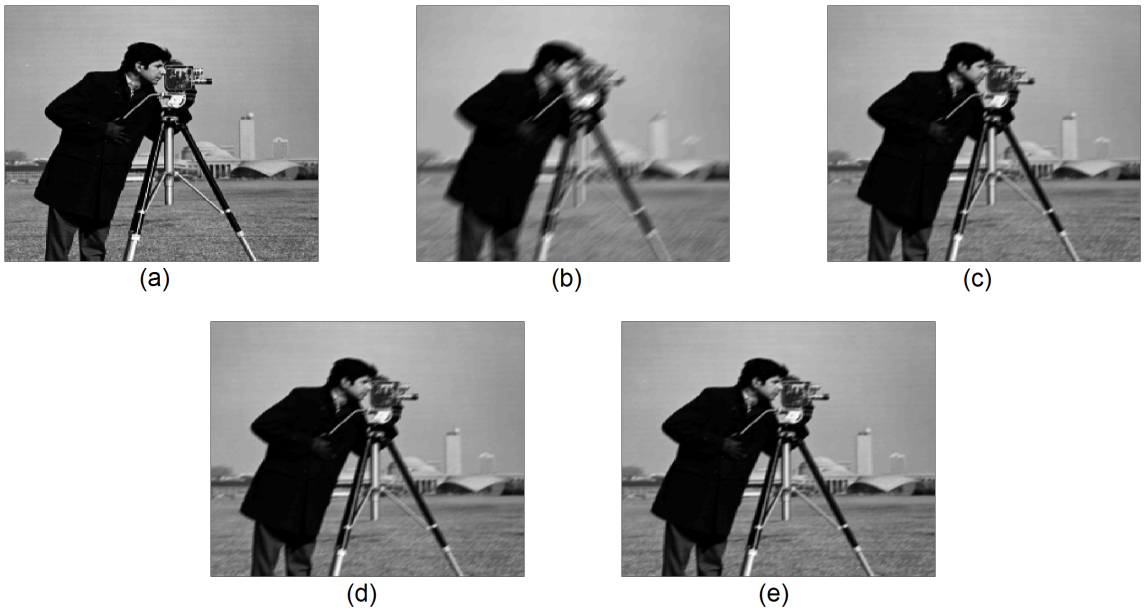

Figure 5. Cameraman image: (a) The original image, (b) the blurred image, (c) the image processed with CGM, (d) the image recovered using TLM method, and (e) the image recovered using the multigrid method.

Table 2. PSNR, iteration count, and CPU time comparison for the Cameraman image.

Cameraman		CGM		Residue		TLM		Residue		Multigrid		Residue
Size	PSNR	Iter.	CPU (s)		PSNR	Iter.	CPU (s)		PSNR	Iter.	CPU (s)	
64×64	23.2052	12	12.2791	1.1176×10^{-8}	26.8332	12	8.5214	7.2134×10^{-8}	24.8792	8	8.5214	9.8389×10^{-9}
128×128	29.1786	25	22.6553	1.1813×10^{-8}	26.8332	27	22.1583	7.3465×10^{-8}	31.1739	17	22.1583	9.8956×10^{-9}
256×256	34.8129	179	98.8374	1.1288×10^{-8}	31.5628	99	77.0612	7.2176×10^{-8}	36.8745	87	77.0612	9.8892×10^{-9}
512×512	45.1752	397	302.2941	1.2913×10^{-8}	42.6923	229	198.1938	7.3455×10^{-8}	47.3441	176	198.1938	9.8916×10^{-9}

Example 3. In this example, the Moon image was used, and the blurring process was performed using the *ke-gen*$(N, 100, 5)$ kernel. The Moon image exhibits prominent texture characteristics. Figure 6 presents different representations of the Moon image, with each subfigure having a resolution of 512×512 pixels. These subfigures include different image processing results with varying methods and parameters. The numerical experiments indicate that the proposed method achieves superior reconstruction quality compared to CGM and TLM. Table 3 summarizes the experimental results.

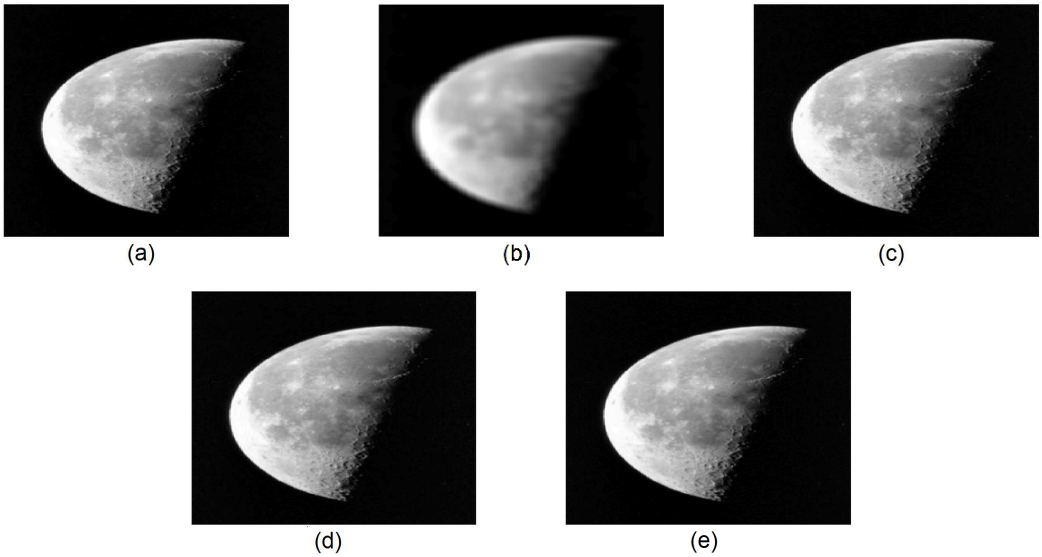

Figure 6. Moon image: (a) The original image, (b) the blurred image, (c) the image processed with CGM, (d) the image recovered using TLM method, and (e) the image recovered using the multigrid method.

Table 3. PSNR, iteration count, and CPU time for the Moon image.

Moon		CGM		Residue		TLM		Residue		Multigrid		Residue
Size	PSNR	Iter.	CPU (s)		PSNR	Iter.	CPU (s)		PSNR	Iter.	CPU (s)	
64×64	59.6722	12	14.2874	1.0243×10^{-8}	51.1398	12	8.7346	7.2344×10^{-8}	61.1263	8	8.7346	9.8136×10^{-9}
128×128	56.8443	25	34.8242	1.0897×10^{-8}	53.8736	23	19.4732	7.1587×10^{-8}	58.2176	17	19.4732	9.7143×10^{-9}
256×256	49.2330	105	97.6345	1.1279×10^{-8}	54.8734	75	45.2735	7.2345×10^{-8}	51.1024	51	45.2735	9.7545×10^{-9}
512×512	45.9967	285	305.2881	1.2169×10^{-8}	56.4235	150	187.8273	7.2355×10^{-8}	47.0132	102	187.8273	9.6734×10^{-9}

Remarks:

1. Figures 4–6 illustrate image quality obtained using different methods. The results indicate that the multigrid method significantly reduces blur and recovers original image with almost same clarity and details.
2. Tables 1–3 show that the proposed approach improves PSNR across all values of N_x.
3. The results demonstrate that the proposed method requires fewer iterations compared to CGM and TLM.
4. Overall, the multigrid approach consistently provides superior performance for image deblurring compared to CGM and TLM.

6. Conclusions

A multigrid method for the total fractional-order variation (TFOV)-based image deblurring problem is proposed. Three examples were evaluated using the proposed technique. For the image deblurring problem, the state and adjoint systems were constructed along with the corresponding optimality conditions. On non-uniform meshes, finite difference approximations were employed, and a multigrid approach on staggered grids was investigated. A preconditioned conjugate gradient method (CGM)

was used as a smoother. The coarsening process with a factor of three produces a hierarchical sequence of staggered grids, which simplifies the intergrid transfer operators and constitutes a key advantage of the proposed multigrid approach. Numerical experiments were conducted on various types of images, including synthetic, real, non-textured, and complex images. The proposed multigrid algorithm was compared with CGM and the two-level method (TLM). The results of the numerical experiments, in terms of peak signal-to-noise ratio and iteration counts, demonstrate that the proposed multigrid method consistently provides improved image reconstruction quality and enhanced computational efficiency.

Author contributions

Shahbaz Ahmad: Conceptualization, data curation, methodology, formal analysis, writing–original draft; Shahid Saleem: Formal analysis, investigation, methodology, validation, writing–original draft; Abid Iqbal: Investigation, software, validation, visualization, writing–review & editing; Saad Arif: Investigation, project administration, supervision, validation, funding acquisition, writing–review & editing. All authors have read and approved the final version of the manuscript for publication.

Funding

This work was supported by the Deanship of Scientific Research, Vice Presidency for Graduate Studies and Scientific Research, King Faisal University, Saudi Arabia [Grant No. KFU261379].

Conflict of interest

All authors declare no conflict of interest in this paper.

References

1. Z. Zhang, L. Zheng, Y. Piao, S. Tao, W. Xu, T. Gao, X. Wu, Blind remote sensing image deblurring using local binary pattern prior, *Remote Sensing*, **14** (2022), 1276. https://doi.org/10.3390/rs14051276
2. G. K. Gultekin, A. Saranli, Feature detection performance based benchmarking of motion deblurring methods: Applications to vision for legged robots, *Image Vision Comput.*, **82** (2019), 26–38. https://doi.org/10.1016/j.imavis.2019.01.002
3. M. S. Hansen, T. S. Sørensen, Gadgetron: An open source framework for medical image reconstruction, *Magn. Reson. Med.*, **69** (2013), 1768–1776. https://doi.org/10.1002/mrm.24389
4. N. Xiong, R. W. Liu, M. Liang, D. Wu, Z. Liu, H. Wu, Effective alternating direction optimization methods for sparsity-constrained blind image deblurring, *Sensors*, **17** (2017), 174. https://doi.org/10.3390/s17010174
5. S. Berhich, N. Moussaid, Non-local blind image deblurring approach using game theory, *Moroccan J. Pure Appl. Anal.*, **10** (2024), 189–204.

6. N. R. Choi, *A comparative study of non-blind and blind deconvolution of ultrasound images*, University of Southern California, 2014.
7. F. E. Salah, N. Moussaid, A. Abassi, *A fractional-order derivative variational framework for blind image deconvolution via nash game strategy*, In: 2024 IEEE 12th International Symposium on Signal, Image, Video and Communications (ISIVC), IEEE, 2024, 1–6. https://doi.org/10.1109/ISIVC61350.2024.10577897
8. C. R. Vogel, M. E. Oman, Fast, robust total variation-based reconstruction of noisy, blurred images, *IEEE T. Image Process.*, **7** (1998), 813–824. https://doi.org/10.1109/83.679423
9. S. Inampudi, S. Vani, R. TB, Image restoration using non-blind deconvolution approach–A comparison, *Int. J. Electron. C. Eng. Technol.*, **10** (2019).
10. S. Tao, W. Dong, H. Feng, Z. Xu, Q. Li, Non-blind image deconvolution using natural image gradient prior, *Optik*, **124** (2013), 6599–6605. https://doi.org/10.1016/j.ijleo.2013.05.068
11. R. Acar, C. R. Vogel, Analysis of bounded variation penalty methods for ill-posed problems, *Inverse Probl.*, **10** (1994), 1217–1229. https://doi.org/10.1088/0266-5611/10/6/003
12. A. N. Tikhonov, Regularization of incorrectly posed problems, *Soviet Math. Dokl*, **4** (1963), 1624–1627.
13. L. I. Rudin, S. Osher, E. Fatemi, Nonlinear total variation based noise removal algorithms, *Physica D*, **60** (1992), 259–268. https://doi.org/10.1016/0167-2789(92)90242-F
14. J. Liu, R. Ma, X. Zeng, W. Liu, M. Wang, H. Chen, An efficient non-convex total variation approach for image deblurring and denoising, *Appl. Math. Comput.*, **397** (2021), 125977. https://doi.org/10.1016/j.amc.2021.125977
15. R. Chan, A. Lanza, S. Morigi, F. Sgallari, An adaptive strategy for the restoration of textured images using fractional order regularization, *Numer. Math.-Theory Me.*, **6** (2013), 276–296. https://doi.org/10.4208/nmtma.2013.mssvm15
16. M. D. Ortigueira, J. J. Trujillo, A unified approach to fractional derivatives, *Commun. Nonlinear Sci.*, **17** (2012), 5151–5157. https://doi.org/10.1016/j.cnsns.2012.04.021
17. A. Ben-Loghfyry, A. Charkaoui, A novel perona-malik model driven by fractional regularized diffusion mechanism with caputo derivative applied to magnetic resonance image processing, *J. Franklin I.*, **362** (2025), 107950.
18. R. Addouch, N. Moussaid, O. Gouasnouane, A. Ben-Loghfyry, Total fractional-order variation and bilateral filter for image denoising, *Math. Model. Comput.*, **11** (2024), 642–653. https://doi.org/10.23939/mmc2024.03.642
19. A. Ben-loghfyry, A. Hakim, Reaction-diffusion equation based on fractional-time anisotropic diffusion for textured images recovery, *Int. J. Appl. Comput. Math.*, **8** (2022), 177.
20. D. Tian, D. Xue, D. Wang, A fractional-order adaptive regularization primal–dual algorithm for image denoising, *Inform. Sciences*, **296** (2015), 147–159. https://doi.org/10.1016/j.ins.2014.10.050
21. J. Zhang, K. Chen, A total fractional-order variation model for image restoration with nonhomogeneous boundary conditions and its numerical solution, *SIAM J. Imaging Sci.*, **8** (2015), 2487–2518. https://doi.org/10.1137/14097121X

22. B. Mathieu, P. Melchior, A. Oustaloup, C. Ceyral, Fractional differentiation for edge detection, *Signal Proc.*, **83** (2003), 2421–2432. https://doi.org/10.1016/S0165-1684(03)00194-4

23. L. Guo, X. L. Zhao, X. M. Gu, Y. L. Zhao, Y. B. Zheng, T. Z. Huang, Three-dimensional fractional total variation regularized tensor optimized model for image deblurring, *Appl. Math. Comput.*, **404** (2021), 126224. https://doi.org/10.1016/j.amc.2021.126224

24. F. Fairag, A. Al-Mahdi, S. Ahmad, Two-level method for the total fractional-order variation model in image, *Numer. Algorithms*, **85** (2020), 931–950. https://doi.org/10.1007/s11075-019-00845-0

25. A. Borzi, V. Schulz, Multigrid methods for pde optimization, *SIAM Rev.*, **51** (2009), 361–395. https://doi.org/10.1137/060671590

26. C. F. Schauf, S. Henn, K. Witsch, Nonlinear multigrid methods for total variation image denoising, *Comput. Visual. Sci.*, **7** (2004), 199–206. https://doi.org/10.1007/s00791-004-0150-3

27. A. Drăgănescu, A. M. Soane, Multigrid solution of a distributed optimal control problem constrained by the stokes equations, *Appl. Math. Comput.*, **219** (2013), 5622–5634. https://doi.org/10.1016/j.amc.2012.11.070

28. S. Takacs, A robust all-at-once multigrid method for the stokes control problem, *Numer. Math.*, **130** (2015), 517–540. https://doi.org/10.1007/s00211-014-0674-5

29. M. M. Butt, A multigrid solver for stokes control problems, *Int. J. Comput. Math.*, **94** (2017), 2297–2314. https://doi.org/10.1080/00207160.2017.1283022

30. S. Saleem, S. Ahmad, J. Kim, Total fractional-order variation-based constraint image deblurring problem, *Mathematics*, **11** (2023), 2869. https://doi.org/10.3390/math11132869

31. K. Ito, K. Kunisch, *Lagrange multiplier approach to variational problems and applications*, SIAM, 2008. https://doi.org/10.1137/1.9780898718614

32. M. D. Ortigueira, Two-sided and regularised riesz-feller derivatives, *Math. Method. Appl. Sci.*, **44** (2021), 8057–8069.

33. C. W. Oosterlee, F. J. G. Lorenz, Multigrid methods for the stokes system, *Comput. Sci. Eng.*, **8** (2006), 34–43. https://doi.org/10.1109/MCSE.2006.115

34. S. Saleem, F. Fairag, A. M. Al-Mahdi, M. M. Al-Gharabli, S. Ahmad, Conformable fractional order variation-based image deblurring, *Part. Differ. Eq. Appl. Math.*, **11** (2024), 100827.

35. X. Ge, J. Tan, L. Zhang, Y. Qian, Blind image deconvolution via salient edge selection and mean curvature regularization, *Signal Proc.*, **190** (2022), 108336. https://doi.org/10.1016/j.sigpro.2021.108336

AIMS Press